PROCEEDINGS OF SPIE

SPIEDigitalLibrary.org/conference-proceedings-of-spie

Fabrication of Si-Au nanocone-nanoparticle array for homogeneous enhancement factor in Raman scattering

K. Srivastava, D. Jonker, M. Lafuente, A. Susarrey-Arce, A. van den Berg, et al.

K. Srivastava, D. Jonker, M. Lafuente, A. Susarrey-Arce, A. van den Berg, Han J. G. E. Gardeniers, W. van der Stam, M. Odijk, "Fabrication of Si-Au nanocone-nanoparticle array for homogeneous enhancement factor in Raman scattering," Proc. SPIE 12197, Plasmonics: Design, Materials, Fabrication, Characterization, and Applications XX, 121970A (3 October 2022); doi: 10.1117/12.2632955

SPIE.

Event: SPIE Nanoscience + Engineering, 2022, San Diego, California, United States

Fabrication of Si-Au nanocone-nanoparticle array for homogeneous enhancement factor in Raman scattering

K. Srivastava[a,b,c], D. Jonker[b,d], M. Lafuente[b,d], A. Susarrey-Arce[b,d], A. van den Berg[a,b,c], Han J.G.E. Gardeniers[b,d] , W. van der Stam[e], M. Odijk[a,b,c]

[a] BIOS Lab on Chip, University of Twente, 7500 AE, Enschede, The Netherlands
[b] MESA+ Institute, University of Twente, 7500 AE, Enschede, The Netherlands
[c] Max Plank Institute of Complex Fluid Dynamics, 7500 AE, Enschede, The Netherlands
[d] Mesoscale Chemical Systems, University of Twente, 7500 AE Enschede, The Netherlands
[e] Inorganic Chemistry and Catalysis, Utrecht University, 3584 CG Utrecht, The Netherlands

ABSTRACT

Gold nanoparticles (AuNPs) were the basis for the earliest research in the field of surface enhanced Raman scattering (SERS). Coupling of their surface plasmon resonances creates hot-spots of high electromagnetic intensities found to be very useful for sensing applications. However, chemically synthesized AuNPs in suspension are usually polydisperse and when arranged on a SERS substrate, lack periodic spatial organization. This leads to large variations in the enhancement factor (EF) which is detrimental to the sensing capabilities of the SERS substrate. Here, we showcase reproducible fabrication of an array of spherical AuNPs at the apices of shell isolated silicon nanocones with a homogeneous EF for SERS. The AuNPs are produced through discrete rotation glancing angle deposition of Au on shell isolated silicon nanocones (SI-SiNC) with square lattice periodicity and 250 nm pitch. By tuning the substrate tilt angle, substrate rotation angle and deposition thickness, the location and the size of the AuNPs formed can be controlled. Using this method, we successfully fabricated 60 nm AuNPs positioned at the apices of the nanocone array. Finite-Difference Time-Domain (FDTD) simulations were performed to visualize the electric field enhancement and verify conditions such as tip radius and oxide shell thickness to optimize the same. The EF was then experimentally calculated by performing SERS measurements on benzenethiol (BT) functionalized AuNPs at 400 unique points over the SI-SiNC substrate and compared to measurements of pure BT solution. A homogeneous substrate EF of $(2.05 \pm 0.05) \cdot 10^7$ (99% confidence interval) at par with literature was calculated for the C-S in-plane deformation mode, δ_{CS}, of the BT molecule excited at 1077 cm^{-1}. Our work highlights the advantages of nanofabrication for homogeneous SERS EF substrates.

Keywords: surface enhanced Raman scattering, plasmonics, silicon nanocones, glancing angle deposition, gold nanoparticle

1. INTRODUCTION

Surface enhanced Raman scattering (SERS) offers the advantage of being a label-free vibrational spectroscopy technique that has been extensively employed in applications such as ultrasensitive detection of chemical and biological compounds[1–3]. Its chemical specificity and resistance to photobleaching makes it an excellent candidate for long term tracking and high-throughput sensing.[4] The SERS phenomenon mainly relies on an electromagnetic mechanism for the enhanced detection of surface bound molecules. Here, the coupling of an electromagnetic wave to the resonance modes present in the SERS substrate (for example: an array of gold nanoparticles (AuNPs)) leads to an increased scattering cross-section of the nanoparticle-molecule complex.[5] As a result, typically low cross-sections in the order of 10^{-30} cm^2sr^{-1} found for Raman scattering can be significantly improved by a few orders of magnitude when using SERS substrates[6]. In addition to the electromagnetic mechanism, a chemical mechanism based on the charge transfer between a chemisorbed molecule and the nanoparticle surface also contributes to the increased polarizability of the nanoparticle-molecule complex.[7] An evident result of the higher scattering cross-section and enhanced nanoparticle-molecule complex polarizability is the increase in the intensity of a specific vibrational band recorded during SERS measurements. This enhancement in the SERS spectra

Plasmonics: Design, Materials, Fabrication, Characterization, and Applications XX, edited by Din Ping Tsai, Takuo Tanaka, Yu-Jung Lu, Proc. of SPIE Vol. 12197, 121970A · © 2022 SPIE
0277-786X · doi: 10.1117/12.2632955

is often represented by a term known as the enhancement factor (EF) which is simply the ratio of the measured SERS intensity to the measured Raman intensity for the specific vibrational band of interest.[6]

With the growing interest in the field and wide range application areas of SERS based sensing, a variety of different methods for the fabrication of SERS substrates have evolved over the years.[8,9] Traditionally used methods include electrochemically roughened metallic films on electrodes and colloidally synthesized metal nanoparticles[5]. The common issue that both these methods struggled with, was the non-uniform enhancement due to variable surface roughness and randomized nanoparticle interaction, respectively. In addition to this, for colloidally synthesized metallic nanoparticles, the complexity in controlling the shape and size of the nanoparticles to ensure uniform distribution was an added task. These metal nanoparticles tended to agglomerate which led to decreased plasmonic activity at some locations, forming cold-spots on the substrate. Whilst at other locations, the very close proximity of the nanoscale features may have led to extremely high electric field hot-spots thereby contributing to the non-uniformity in the SERS EF. In such a scenario, for low concentrations, bonding of an analyte molecule to a cold-spot is undesirable.

To improve on the inherent drawbacks of the above mentioned chemical synthesis routes, lithographic fabrication has emerged as an excellent tool to fabricate uniform SERS substrates with a variety of shapes, geometries and other physical parameters such as periodicity, width and height of the nanostructures[1,10]. Some of the commonly used techniques include electron beam lithography (EBL)[11–14], laser interference lithography (LIL)[15–18], nanosphere lithography (NSL)[19–22] and nanoimprint lithography (NIL)[23–26]. Amongst all these techniques, displacement talbot lithography (DTL)[27] for SERS substrate fabrication has also developed as an innovative method of fabrication[28,29]. Employing a variety of lithographic processes undoubtedly provides one with the opportunity to manipulate the physical and geometric parameters that significantly influence the EF. However, the time consideration and manual effort put into designing and fabricating various nanostructures in order to find the optimal parameters can be a cumbersome process. Many researchers therefore use numerical methods to simulate such conditions[30]. This has a three-fold benefit; 1) it provides a deeper understanding of the physical phenomenon contributing to the SERS enhancement 2) it serves as a tool to fine-tune the physical parameters contributing to SERS enhancement and lastly 3) it can also be used as a base to compare theoretical and experimental results although it should be noted that simulations only take into account the enhancement arising from the electromagnetic effect.[30,31]

In this work, we report the fabrication of a Si-Au nanocone-nanoparticle array with homogeneous SERS activity and EFs of 7 orders of magnitude. First, the oxide shell isolated silicon nanocones (SI-SiNC) are fabricated using DTL and then the AuNPs are deposited using discrete rotation glancing angle deposition (DR-GLAD). Using this combination, positioning of the AuNPs at the apex of the SI-SiNC is obtained. We report a homogeneous SERS EF of $(2.05 \pm 0.05) \cdot 10^7$ for the AuNP@SI-SiNC arrays functionalized with benzenethiol (BT). To further shape the AuNPs, the Si-Au nanocone-nanoparticles arrays are annealed for which no experimental enhancement was observed. In order to gain more insight on this problem, numerical simulations using Finite Difference Time Domain (FDTD) were conducted where the impact of different annealing conditions on the SERS enhancement is evaluated. The simulation results revealed that the gradual annealing of the SI-SiNCs represented by an increasing oxide shell thickness leads to a decrease in the electromagnetic enhancement observed for the AuNP@SI-SiNC arrays. For the same oxide shell thickness however, increasing the tip radius of the nanocone did not have any noticeable impact on the enhancement.

2. EXPERIMENTAL

2.1 Fabrication

The SI-SiNC were fabricated using DTL as reported by Jonker et al[29]. The SI-SiNC used in this work have a thermally grown 5 nm oxide shell around them. Au deposition was then performed on the SI-SiNCs using a thermal evaporator (BAK 600). It is a high vacuum deposition system that uses a high volage electron beam for resistive heating of Au, thereby generating a vapor flux. The substrate holder in this system is capable of thin film metal deposition at various tilt and rotational angles. Tilt angle (θ) here is the angle between the vapor flux and the substrate normal. The rotational angle (φ) is the circular rotation of the substrate, perpendicular to the substrate normal. For a quadruple deposition, the substrate is rotated three times with $\varphi = 90^\circ$ for each successive deposition. The deposition was carried out at a rate of 0.1 nm/s with a vacuum pressure in the order of 10^{-7} torr. A beam current of 280-320 mA was used for the deposition.

2.2 Thermal annealing

To shape the spherical AuNPs, a proportional-integral-differential controlled furnace (TSD-12 furnace, Toma, Netherlands) was used for thermal annealing. Two different reaction conditions (i.e annealing temperature and time) were used to monitor the size, shape and location of the AuNP formed. Annealing was conducted at 1000˚C for 60 mins, excluding a ramp up and ramp down time of 60 mins, additionally. All annealing experiments were conducted in ambient air. The fabrication process flow is shown in Figure 1(a).

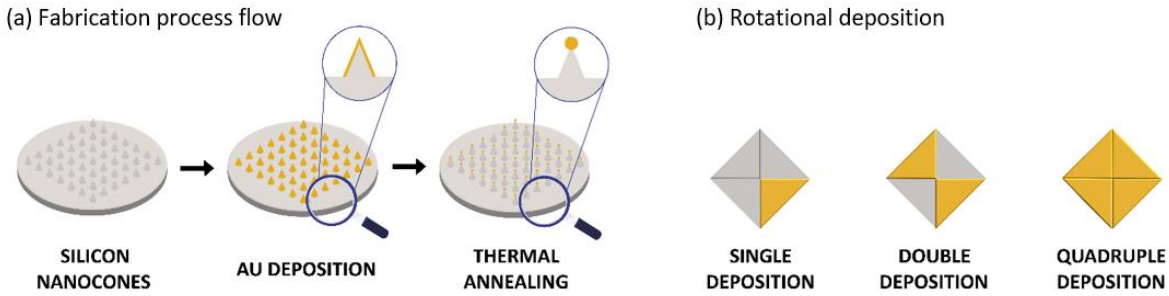

Figure 1: (a) Process flow for fabrication Si-Au nanocone-nanoparticle arrays. (b) Top view; glancing angle deposition at different nanocone faces leading to single, double and quadruple deposition.

2.3 Spectroscopy measurements

Reflectance measurements were performed on a Leica DM6000 FS microscope (Ocean Optics HR4000 detector and bright light source Leica type 11307072960). All reflectance intensities measured were normalized by the maximum value in the silicon reference data set.

A WITec Alpha300R Raman microscope with a UHTS 300 spectrometer was used to perform Raman and SERS measurements. The specifications include: a 633 nm excitation wavelength and a lens of 100x magnification with a numerical aperture of 0.9. An edge filter was used to filter the backscatter electrons from the excitation beam and the directed photons were guided towards an MCT detector cooled at -60˚C. An integration time of 3s with a laser power of 2mW was kept constant for all measurements. An averaged data spectrum was used for analysis (n=10). Finally, a 5µm x 5µm scan area of the nanocone-nanoparticle array was subjected to square mapping. Here, the enhancement factor (AEF) was calculated for 400 measurements (20 lines x 20 lines). Benzenethiol (BT, Thermo Scientific 99%) was chosen as a probe molecule. The samples were immersed in a 10mM BT in ethanol solution overnight and then rinsed with fresh ethanol. For reference measurements, a Raman spectra of a pure BT under the same experimental conditions was used. The SERS spectra were smoothed by a moving average window with window-size three after which they were baseline corrected, using the asymmetrically reweighted penalized least squares smoothing algorithm introduced by Baek et al.[32] Normalization was conducted after baseline correction by taking the ratio with the maximum value present in individual recorded spectra.

2.4 FDTD simulations

Numerical simulations were conducted with Ansys Lumerical 2022 R1 Finite Difference IDE. Various nanocone and oxide shell geometries were designed in Solidworks and STL files were imported to Lumerical. The SI-SiNC dimensions used in the model were measured from images recorded through a Scanning Electron Microscope (SEM). A 3D-FDTD simulation domain of 250 nm × 250 nm × 2µm (x,y,z) was created around the SI-SiNC and an AuNP with a 30 nm radius was placed at the apex of the nanocone. Palik model was used to set the material properties of Si, SiO_2 and Au.[33] The simulations were conducted at a mesh accuracy of 2 and a mesh size of 0.2 nm. A plane wave source with wavelength ranging from 400-800 nm was placed 1 µm above the AuNP@SI-SiNC geometry. Normalized electric field intensity was collected using frequency domain field and power monitors at the cross-section of the AuNP@SI-SiNC. This data was recorded at 633 nm laser wavelength. Post-processing of the enhancement images obtained from the simulations was performed in MATLAB.

3. RESULTS AND DISCUSSION

3.1 Fabrication

Table 1 summarizes the different experiments that were conducted on the SI-SiNC arrays along with their DR-GLAD and annealing parameters.

Table 1. Fabrication parameters – Au deposition on SI-SiNC to form AuNP@SI-SiNC arrays

Sample Name	Au thickness (nm)	Tilt angle (degrees)	No. of depositions	Annealing temp (˚C)	Annealing time (mins)
QD-A_0	10	85	4	-	-
QD-A_{1000}	10	85	4	1000	60

Samples QD-A_0 and QD-A_{1000} were subjected to four depositions at a glancing angle of 85˚. For simplicity, we assumed that the nanocones used in this work had four faces as shown in Figure 1(b) and three successive discrete 90˚ rotations were performed between the four depositions. QD-A_{1000} was further annealed at 1000˚C. Annealing is a widely used method to reshape thin films in order to form nanoparticles.[34–36] However, a major obstacle often highlighted when using this method, is the lack of control over the random size and location distribution of the nanoparticles formed. This often reduces the sensitivity of the plasmonic effect[37]. On the other hand, combining GLAD with annealing offers the advantage of selective deposition on nanostructure surfaces. This leads to better controlled and uniform nanoparticle distributions when substrates are subjected to annealing. In our case, the efficient use of GLAD leads to the selective deposition of Au at the nanocone apex which gets further transformed into a spherical particle upon annealing. The results of the deposition and the annealing experiments can be found in the SEM images in Figure 2. It can be seen that even without annealing for QD-A_0, spherical AuNP formation takes place on top of the nanocone array when four sequential depositions at a glancing angle of 85˚ are conducted. The AuNP array formed is highly ordered with a diameter of 67 ± 6 nm. For QD-A_{1000}, it is interesting to see the formation of faceted AuNPs. In addition to this, some of the AuNPs also migrate away from the SI-SiNC apices. Heating up- or close- to the melting point of Au followed by a relatively slow cooling down cycle yields the facetted appearance of the obtained AuNPs.[38] These morphological transitions also depend on the size of the nanoparticle and the maximum temperature of the annealing cycle.[39] Furthermore, oxidation of SI-SiNCs is observed. Here, the SI-SiNCs convert to SiO_2 nanocones upon annealing in ambient air. This effect can be dominantly observed from the expansion of the nanocone in the SEM image for QD-A_{1000}, as conversion of Si into SiO_2 is accompanied by volumetric expansion and constrained by stress generated at the Si-SiO_2 interface pronounced in concave and convex corners. An etching test in hydrofluoric acid confirmed the complete conversion into SiO_2 as all cones were consumed by the hydrofluoric acid, if they were subjected to an annealing cycle.

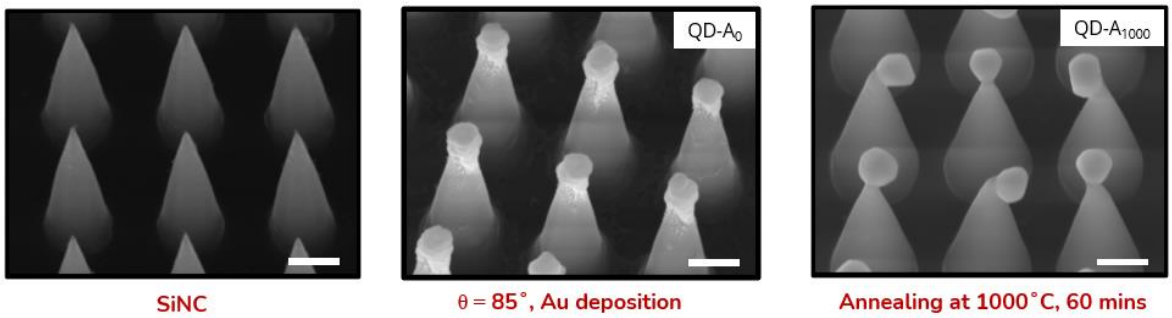

Figure 2: SEM images of AuNP@SI-SiNC; QD-A_0: SI-SiNC subjected to quadruple deposition at $\theta = 85^\circ$, QD-A_{1000}SI-SiNC subjected to quadruple deposition at $\theta = 85^\circ$ and annealed at 1000˚C; scale bar = 100 nm

3.2 Reflectance and Raman measurements

Optical characterization of the fabricated samples was performed by measuring the reflectance spectra of the SI-SiNCs, the two AuNP@SI-SiNC geometries and a Si substrate reference. Figure 3 shows the measured reflectance intensities for

mentioned samples, respectively. An appearance of a dip in the spectrum at 520 nm characterized by a decreased reflectance intensity can be correlated to the SI-SiNC geometry[40]. This can also be confirmed from the observation that this feature is present in the plot for both SI-SINC and QD-A_0. Interestingly, the reflectance spectrum of QD-A_{1000} appears to be very different from QD-A_0 and the characteristic nanocone feature at 520 nm is also not present anymore. These results imply that the SI-SiNCs underwent a morphological change when annealed which contributes to the disappearance of the characteristic nanocone feature.

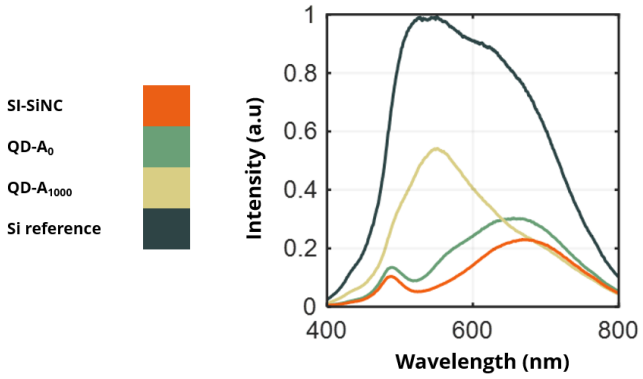

Figure 3: Reflectance measurements for SI-SiNC, QD-A_0, QD-A_{1000} and Si reference

In order to characterize the SERS activity of the fabricated AuNP@SI-SiNC arrays, the SERS signals recorded over the BT functionalized AuNP@SI-SiNC arrays were compared to the Raman signal of pure BT solution. From Figure 4 (a), it can be seen that an increase in the number of detected peaks and their relative magnitude is recorded for QD-A_0 when compared to the spectra for pure BT. An increase in the number of detected BT peaks showcases the SERS capability of the AuNP@SI-SiNC array to sensitively distinguish between the different BT characteristic peaks. Interestingly, Raman peaks of BT are absent for QD-A_{1000}. Further investigation of this sample will be covered in the following section.

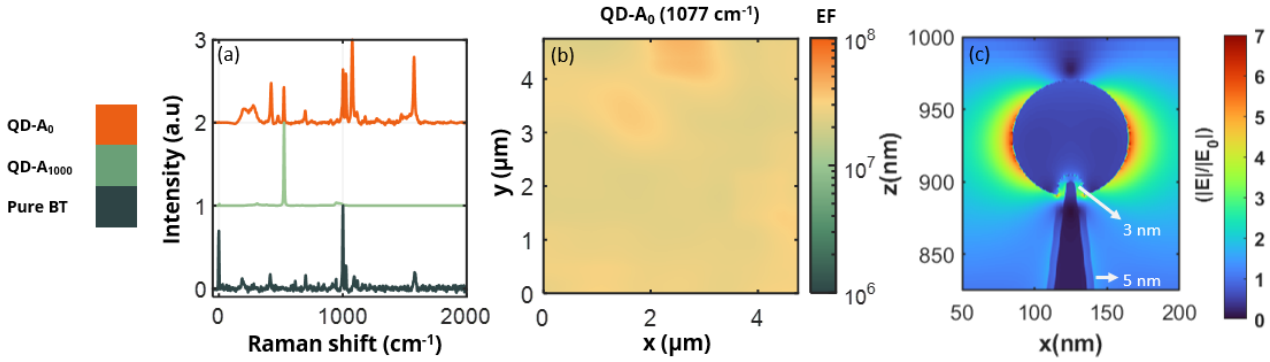

Figure 4: (a) SERS signals for QD-A_0, QD-$A_{1000}$and Raman signal of pure BT; (b) AEF map for a 25μm^2 area of the AuNP@SI-SiNC array – QD-A_0; (c) FDTD simulated image of the electric field intensity distribution for AuNP@SI-SiNC with tip radius = 3 nm and oxide shell thickness = 5 nm – QD-A_0 at 633 nm wavelength

The SERS activity of QD-A_0 was calculated through the EF using the following equation[41,42]:

$$EF = \frac{I_{SERS}/N_{SERS}}{I_{Raman}/N_{Raman}}$$

Where I_{SERS} is the integrated intensity of the selected peak for the SERS substrate whereas I_{RAMAN} is the integrated intensity of the same peak in a neat BT solution. The intensity ratio is then normalized to the number of probed molecules in the SERS substrate (N_{SERS}) and the neat BT solution (N_{RAMAN}). All calculations were performed for the Au-BT peak shifted at 1077 cm^{-1} which represents the C-S in-plane deformation mode, δ_{Cs} of BT. It should be noted that since QD-A_{1000} did not show any SERS enhancement, the EF in this case was not calculated.

The uniformity of the SERS substrate was assessed by measuring a surface map of 5 µm x 5 µm with 400 data points. The EF was calculated at each data point as seen in Figure 3 (b) which revealed a mean value of $2.25 \pm 0.05 \cdot 10^7$ with only 10% variation over the entire substrate. The low amount of variance in the observed mean EF correlates to the low amount of variance observed in the fabricated AuNP@SI-SiNC structure with an AuNP diameter of 67±6 nm. The observed uniformity in the mean EF might facilitate an improved platform for low concentration (micro and nanomolar) analyte detection due to the relatively large probability of the analyte bonding to a hot-spot. Figure 3(c) depicts the electromagnetic hot-spot formation around the AuNP for a AuNP@SI-SiNC geometry. It can be seen that the highest value for the normalized electric field intensity is recorded at the AuNP hot-spot while a gradual decline in the electric field intensity is observed when moving radially away from the AuNP surface. This correlates to the fact that SERS enhancement is a surface phenomenon, where the highest electric field intensities are recorded closest to the nanostructure surface, often within the range of 2-10 nm[43]. The AuNP@SI-SiNC simulated here consists of a 60 nm AuNP apexed at a SI-SiNC with an oxide shell thickness of 5 nm and a tip radius of 3 nm.

3.3 Impact of annealing and tip curvature

We hypothesize that the annealing process had an impact on the SERS performance of QD-A_{1000}. When the nanocones are annealed, the change in the refractive index of the material may have altered the interaction of Raman light with the AuNP, which is now apexed on a complete silica (SiO_2) nanocone instead of a SI-SiNC. In addition to this, from the SEM images in Figure 2, it can also be observed that the nanocone grows in width from 100 nm to 116 nm, changing the spacing between the nanocones even though the periodicity remains the same. As it was mentioned before, parameters such a shape, size and spatial organization of nanostructures play a crucial role in the far-field interactions that give rise to local electromagnetic enhancement. Therefore, the modification of the material composition and the dimensions of the nanostructures may have had a drastic impact on the SERS enhancement.

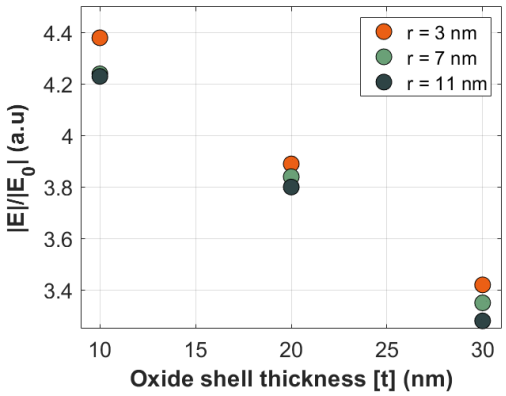

Figure 5: FDTD-simulated electromagnetic field versus SI-SiNC oxide shell thickness (t) for three different radius of the cone tip (r).

In order to test the hypothesis, FDTD simulations were performed to understand the influence of SiO_2 shell thickness, (t) and variations in the nanocone apex radius of curvature, (r), on the electric field distribution. From SEM and TEM images in previously reported work[29], it was found that these dimensions for SI-SiNCs used in this work experimentally are close to t = 5 nm and r = 3 nm. Therefore, it was interesting to perform simulations considering a larger domain for t and r, and hence, simulations with t = 10, 20 and 30 nm for different cone-tip radius (r = 3, 7 and 11 nm) were conducted to characterize variations in local electric field.

Figure 5 shows the maximum normalized electric field enhancement as a function of the oxide shell thickness (t) calculated for three different radii of the cone tip (r). It can be clearly seen that the intensity is found to be highest for the case with the thinnest SI-SiNC shell (t = 10nm). Comparing the intensity for SI-SiNC with a fixed tip radius of 3 nm and t = 5 nm (see Figure 4 (c)) and t = 10 nm (see Figure 6), a drastic decrease in the normalized electric field intensity can already be observed when comparing the color bars. Moreover, a further decrease in the intensity is observed when the oxide shell thickness is increased from 10 nm to higher values such as 20 and 30 nm as seen in Figure 5. Insight gained from these simulations contribute to the hypothesis that the oxidation of the SI-SiNCs leads to a decrease in the normalized electric field enhancement which might be an indication as to why QD-A_{1000} does not show any SERS signals for BT as seen in Figure 4(a). From Figure 5, it can be seen that changing the oxide shell thickness has a more pronounced effect on the

simulated SERS enhancement, but that this change is much less when the tip radius is varied. Increasing the tip radius has only a very small negative effect on the SERS enhancement. Figure 6 includes the simulated insets of different geometries of SI-SiNC obtained when the radius of curvature is increased from 3 nm to 11 nm for each corresponding oxide shell thickness. Here, the oxide shell thickness is varied from 10 nm to 30 nm with an increasing step size of 10 nm.

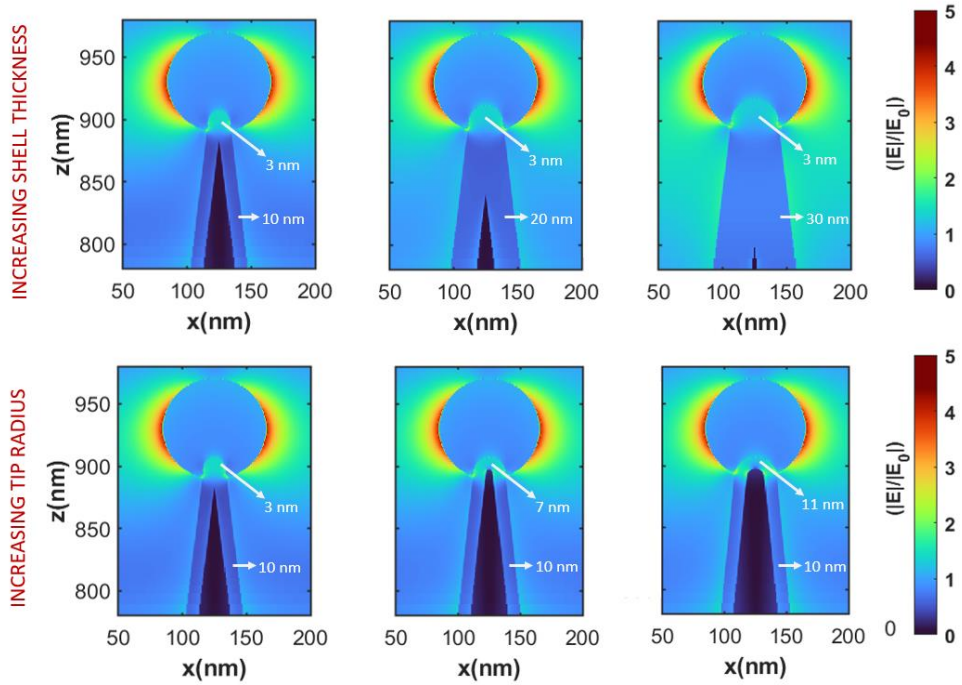

Figure 6: (a) FDTD simulated distribution of the local field intensity at an excitation wavelength of 633 nm for SI-SiNC oxide shell variation, t = 10, 20 and 30 nm for r = 3 nm (b) SI-SiNC tip radii variation, r = 3, 7, 11 nm for t = 10 nm

4. CONCLUSION

In this work, we report the fabrication of a AuNP@SI-SiNC array for Raman scattering enhancement. Here, the GLAD played a crucial role in the fabrication and positioning of the AuNPs at the apices of the SI-SiNC arrays. Thermal annealing was additionally employed to further shape the as-deposited AuNPs to obtain a more spherical geometry. Two samples were thus fabricated and characterized which were further subjected to BT functionalization to calculate a SERS EF. Based on experimental SERS signals obtained, it was observed that only the as-deposited sample with no annealing treatment (QD-A_0) showed SERS enhancement. For samples annealed 1000˚C (QD-A_{1000}), no SERS enhancement was recorded. Focusing on QD-A_0, a homogeneous EF of $(2.05 \pm 0.05) \cdot 10^7$ was calculated for the C-S vibrational stretching at 1077 cm^{-1}. The SERS EF showed only 10% variation throughout the substrate as revealed from a square mapping performed on a 25 μm^2 area. To gain a better understanding of the physical and geometrical parameters influencing the SERS enhancement, FDTD simulations were performed to visualize and quantify the electric field enhancement. In these simulations, the impact of annealing on the AuNP@SI-SiNC arrays was explored by increasing the oxide shell thickness in each subsequent simulation. Moreover, the influence of radius of curvature of the nanocone tip on the enhancement was also recorded. The results from the simulations strengthen our hypothesis that when the AuNP@SI-SiNC arrays are annealed, the electromagnetic interactions change due to the change in the material and geometric composition of the nanocone. The oxidation of the nanocone leads to a thicker oxide shell formation which causes the electric field intensity to decrease significantly. Simulations confirm that further oxidation of the nanocones only results in decreasing electric field intensity.

ACKNOWLEDGEMENTS

This work was supported by the Netherlands Center for Multiscale Catalytic Energy Conversion (MCEC) and the Netherlands Organisation for Scientific Research (NWO) Gravitation programme funded by the Ministry of Education, Culture and Science of the government of the Netherlands. [Grant No. 801359]

REFERENCES

1. Fan M, Andrade GFS, Brolo AG. A review on the fabrication of substrates for surface enhanced Raman spectroscopy and their applications in analytical chemistry. *Anal Chim Acta*. 2011;693(1-2):7-25. doi:10.1016/j.aca.2011.03.002
2. Ambartsumyan O, Gribanyov D, Kukushkin V, Kopylov A, Zavyalova E. SERS-based biosensors for virus determination with oligonucleotides as recognition elements. *Int J Mol Sci*. 2020;21(9):1-15. doi:10.3390/ijms21093373
3. Radziuk D, Moehwald H. Prospects for plasmonic hot spots in single molecule SERS towards the chemical imaging of live cells. *Phys Chem Chem Phys*. 2015;17(33):21072-21093. doi:10.1039/c4cp04946b
4. Gu X, Trujillo MJ, Olson JE, Camden JP. SERS Sensors: Recent Developments and a Generalized Classification Scheme Based on the Signal Origin. *Annu Rev Anal Chem*. 2018;11(March):147-169. doi:10.1146/annurev-anchem-061417-125724
5. Betz JF, Yu WW, Cheng Y, White IM, Rubloff GW. Simple SERS substrates: Powerful, portable, and full of potential. *Phys Chem Chem Phys*. 2014;16(6):2224-2239. doi:10.1039/c3cp53560f
6. Le Ru EC, Blackie E, Meyer M, Etchegoint PG. Surface enhanced raman scattering enhancement factors: A comprehensive study. *J Phys Chem C*. 2007;111(37):13794-13803. doi:10.1021/jp0687908
7. Wang X, Huang SC, Hu S, Yan S, Ren B. Fundamental understanding and applications of plasmon-enhanced Raman spectroscopy. *Nat Rev Phys*. 2020;2(5):253-271. doi:10.1038/s42254-020-0171-y
8. Liu X, Guo J, Li Y, et al. SERS substrate fabrication for biochemical sensing: Towards point-of-care diagnostics. *J Mater Chem B*. 2021;9(40):8378-8388. doi:10.1039/d1tb01299a
9. Li C, Huang Y, Li X, et al. Towards practical and sustainable SERS: a review of recent developments in the construction of multifunctional enhancing substrates. *J Mater Chem C*. 2021;9(35):11517-11552. doi:10.1039/d1tc02134f
10. Kasani S, Curtin K, Wu N. A review of 2D and 3D plasmonic nanostructure array patterns: Fabrication, light management and sensing applications. *Nanophotonics*. 2019;8(12):2065-2089. doi:10.1515/nanoph-2019-0158
11. Chang YC, Huang BH, Lin TH. Surface-enhanced Raman scattering and fluorescence on gold Nanogratings. *Nanomaterials*. 2020;10(4). doi:10.3390/nano10040776
12. Zheng M, Zhu X, Chen Y, Xiang Q, Duan H. Three-dimensional donut-like gold nanorings with multiple hot spots for surface-enhanced raman spectroscopy. *Nanotechnology*. 2017;28(4):1-7. doi:10.1088/1361-6528/28/4/045303
13. Yue W, Gong T, Long X, et al. Sensitive and reproducible surface-enhanced raman spectroscopy (SERS) with arrays of dimer-nanopillars. *Sensors Actuators, B Chem*. 2020;322(April). doi:10.1016/j.snb.2020.128563
14. Huebner U, Boucher R, Schneidewind H, Cialla D, Popp J. Microfabricated SERS-arrays with sharp-edged metallic nanostructures. *Microelectron Eng*. 2008;85(8):1792-1794. doi:10.1016/j.mee.2008.05.005
15. Van Rijn CJM. Laser interference as a lithographic nanopatterning tool. *J Microlithogr Microfabr Microsystems*. 2006;5(1):1-6. doi:10.1117/1.2173269
16. Zhang X, Strauf S. Formation of triplet and quadruplet plasmonic nanoarray templates by holographic lithography. *Appl Phys Lett*. 2013;102(9). doi:10.1063/1.4794840
17. Xu B Bin, Ma ZC, Wang H, et al. A SERS-active microfluidic device with tunable surface plasmon resonances. *Electrophoresis*. 2011;32(23):3378-3384. doi:10.1002/elps.201100309
18. Chen HM, Pang L, Huang GM, Cambrea L, Fainman Y. Two-dimensional, periodic mushroomlike nanostructures for SERS applications. *Nanoscale Imaging, Sensing, Actuation Biomed Appl VIII*. 2012;8231(February 2012):82310T-82310T - 6. doi:10.1117/12.909591
19. Zhang X, Yonzon CR, Van Duyne RP. Nanosphere lithography fabricated plasmonic materials and their applications. *J Mater Res*. 2006;21(5):1083-1092. doi:10.1557/jmr.2006.0136
20. Wang TJ, Hsu KC, Liu YC, Lai CH, Chiang HP. Nanostructured SERS substrates produced by nanosphere lithography and plastic deformation through direct peel-off on soft matter. *J Opt (United Kingdom)*. 2016;18(5). doi:10.1088/2040-8978/18/5/055006
21. Chau YFC, Chen KH, Chiang HP, et al. Fabrication and characterization of a metallic–dielectric nanorod array by nanosphere lithography for plasmonic sensing application. *Nanomaterials*. 2019;9(12). doi:10.3390/nano9121691
22. Hulteen JC, Van Duyne RP. Nanosphere lithography: A materials general fabrication process for periodic particle array surfaces. *J Vac Sci Technol A Vacuum, Surfaces, Film*. 1995;13(3):1553-1558. doi:10.1116/1.579726
23. Guo LJ. Nanoimprint lithography: Methods and material requirements. *Adv Mater*. 2007;19(4):495-513. doi:10.1002/adma.200600882
24. Ryu Y, Kang G, Lee CW, Kim K. Porous metallic nanocone arrays for high-density SERS hot spots via solvent-

assisted nanoimprint lithography of block copolymer. *RSC Adv*. 2015;5(93):76085-76091. doi:10.1039/c5ra11787a
25. Alvarez-Puebla R, Cui B, Bravo-Vasquez JP, Veres T, Fenniri H. Nanoimprinted SERS-active substrates with tunable surface plasmon resonances. *J Phys Chem C*. 2007;111(18):6720-6723. doi:10.1021/jp070906s
26. Wu W, Hu M, Ou FS, Li Z, Williams RS. Cones fabricated by 3D nanoimprint lithography for highly sensitive surface enhanced Raman spectroscopy. *Nanotechnology*. 2010;21(25). doi:10.1088/0957-4484/21/25/255502
27. Solak HH, Dais C, Clube F. Displacement Talbot lithography: a new method for high-resolution patterning of large areas. *Opt Express*. 2011;19(11):10686. doi:10.1364/oe.19.010686
28. Le-The H, Lozeman JJA, Lafuente M, et al. Wafer-scale fabrication of high-quality tunable gold nanogap arrays for surface-enhanced Raman scattering. *Nanoscale*. 2019;11(25):12152-12160. doi:10.1039/c9nr02215e
29. Jonker D, Berenschot EJW, Tiggelaar RM, Tas NR, Van Houselt A, Gardeniers HJGE. A Self-Aligned Wafer-Scale Gate-All-Around Aperture Definition Method for Silicon Nanostructures. *IEEE Symp Mass Storage Syst Technol*. 2022;2022-Janua(January):561-564. doi:10.1109/MEMS51670.2022.9699565
30. Zeng Z, Liu Y, Wei J. Recent advances in surface-enhanced raman spectroscopy (SERS): Finite-difference time-domain (FDTD) method for SERS and sensing applications. *TrAC - Trends Anal Chem*. 2016;75:162-173. doi:10.1016/j.trac.2015.06.009
31. Stiles PL, Dieringer JA, Shah NC, Van Duyne RP. Surface-enhanced Raman spectroscopy. *Annu Rev Anal Chem*. 2008;1(1):601-626. doi:10.1146/annurev.anchem.1.031207.112814
32. Baek S-J, Park A, Ahn Y-J, Choo J. Baseline correction using asymmetrically reweighted penalized least squares smoothing. *Analyst*. 2015;140(1):250-257. doi:10.1039/c4an01061b
33. Palik ED. Handbook of Optical Constants of Solids. *Acad Press*. Published online 1998.
34. Lee FY, Fung KH, Tang TL, Tam WY, Chan CT. Fabrication of gold nano-particle arrays using two-dimensional templates from holographic lithography. *Curr Appl Phys*. 2009;9(4):820-825. doi:10.1016/j.cap.2008.07.017
35. Barman B, Dhasmana H, Verma A, Kumar A, Chaudhary SP, Jain VK. Formation of plasmonic silver nanoparticles using rapid thermal annealing at low temperature and study in reflectance reduction of Si surface. *Adv Nat Sci Nanosci Nanotechnol*. 2017;8(3). doi:10.1088/2043-6254/aa7252
36. Purwidyantri A, El-Mekki I, Lai CS. Tunable Plasmonic SERS Hotspots on Au-Film over Nanosphere by Rapid Thermal Annealing. *IEEE Trans Nanotechnol*. 2017;16(4):551-559. doi:10.1109/TNANO.2016.2647263
37. Lin HTH, Yang CK, Lin CC, Wu AMH, Wang LA, Huang NT. A large-area nanoplasmonic sensor fabricated by rapid thermal annealing treatment for label-free and multi-point immunoglobulin sensing. *Nanomaterials*. 2017;7(5). doi:10.3390/nano7050100
38. Müller CM, Mornaghini FCF, Spolenak R. Ordered arrays of faceted gold nanoparticles obtained by dewetting and nanosphere lithography. *Nanotechnology*. 2008;19(48). doi:10.1088/0957-4484/19/48/485306
39. Koga K, Ikeshoji T, Sugawara KI. Size- and Temperature-Dependent Structural Transitions in Gold Nanoparticles. *Phys Rev Lett*. 2004;92(11):2-5. doi:10.1103/PhysRevLett.92.115507
40. Kristensen A. Raman scattering in high-refractive-index nanostructures. 2021;10(4):1197-1209.
41. Pilot R, Bozio R. Validation of SERS enhancement factor measurements. *J Raman Spectrosc*. 2018;49(3):462-471. doi:10.1002/jrs.5302
42. Lin XM, Cui Y, Xu YH, Ren B, Tian ZQ. Surface-enhanced raman spectroscopy: Substrate-related issues. *Anal Bioanal Chem*. 2009;394(7):1729-1745. doi:10.1007/s00216-009-2761-5
43. Langer J, de Aberasturi DJ, Aizpurua J, et al. Present and future of surface-enhanced Raman scattering. *ACS Nano*. 2020;14(1):28-117. doi:10.1021/acsnano.9b04224